EXPERIMENTAL INVESTIGATIONS OF INHOMOGENEOUS COMPONENT PROPERTIES IN LASER-BASED ADDITIVE MANUFACTURING OF AlSi10Mg

S. Czink*, V. Schulze* and S. Dietrich*

*Institute of Applied Materials, Karlsruhe Institute of Technology (KIT), Karlsruhe, Germany

Abstract

In the laser-based additive manufacturing (PBF-LB) process of AlSi10Mg components, the layer-by-layer deposition leads to microscopic and macroscopic thermal effects (shrinkage, residual stresses, overheating) depending on the component geometry. This results in a strong dependence of the microstructure and therefore of the process-induced material properties on the shape of the manufactured component. To analyze this behavior, components with different geometric aspects, such as various construction angles, were built using the PBF-LB process. In order to perform a spatially-resolved characterization and evaluation of the mechanical behavior of the component, small-scale tensile specimens in the sub-millimeter range were manufactured from representative areas of the components. With the obtained results, design approaches based on local material data can be improved significantly.

Introduction

Due to the high degree of individualization and design flexibility, additive manufacturing techniques, such as the laser based powder bed fusion (PBF-LB), have developed from rapid prototyping to established rapid manufacturing processes. In the PBF-LB process, the components are built incrementally by local melting of metal powder with a focused laser beam. This enables the manufacturing of geometrically complex parts, such as lattice structures or topology optimized components in a single step. One of the most common alloys for the PBF-LB process is AlSi10Mg. Its composition close to the eutectic of the ternary system Al-Si-Mg leads to a good castability in comparison to other aluminum alloys. Due to the combination of good mechanical properties with a low density, the alloy is suitable for applications in lightweight design. Additionally, PBF-LB parts out of AlSi10Mg show similar or even superior mechanical properties compared to traditional casting due to the unique microstructure of the PBF-LB parts. The microstructure is coupled to the high cooling rates in the process of up to 10^6 K/s [1]. This results in an ultrafine cellular microstructure with primary crystallized Al and a fibrous eutectic Si network at the cell boundaries [2, 3]. However, different processing parameters can influence the cooling conditions and therefore the resulting microstructure [4]. Several studies additionally investigated the influence of the component geometry on the resulting microstructure. For example, Dong et al. studied the change of microstructure for cylindrical AlSi10Mg samples of different sizes [5]. Liu investigated the microstructure and hardness for lattice structures of AlSi10Mg [6]. The study showed that due to the isolating effect of surrounding powder particles at downskin surfaces of overhanging samples the cooling behavior is influenced locally, which leads to a gradient regarding the microstructure. Yue et al. analyzed this effect with a finite element model and found that the melt pools have a higher size and temperature towards the downskin surface of overhanging structures [7]. In addition to the microstructure, the formation of defects can also be influenced by

the component geometry. Englert et al. showed an increase in keyhole porosity at downskin surfaces at overhanging structures, especially during processing at lower scanning speeds [8].
Within this work, the effect of an inhomogeneous microstructure on the mechanical properties of AlSi10Mg parts were studied. Therefore, representative specimens of different sizes were built with the PBF-LB process under different construction angles. The effects of the microstructure on the local mechanical behavior were evaluated using small-scale tensile bars prepared from the representative specimens. To analyze the influence of the locally inhomogeneous microstructure on the global component behavior, the mechanical properties of a topology optimized component were tested.

Sample Processing

Material

AlSi10Mg powder supplied by m4p materials solutions GmbH (Feistritz i.R., Austria) with a powder bulk density of 1.51 g/cm³ served as base material. Table 1 shows the chemical composition of the powder with a size distribution of D_{10} = 20.5 µm, D_{50} = 33.9 µm and D_{90} = 56.8 µm.

Table 1: Chemical composition of the AlSi10Mg powder particles in wt.%.

Al	Fe	Si	Mg	Mn	Ti	Zn	Cu	Pb	Sn	Ni
Base	0.16	10.5	0.31	<0.01	<0.01	<0.01	<0.01	<0.01	<0.01	<0.01

PBF-LB system

The bulk material, which was analyzed in this study, was manufactured with a Creator from O.R. Lasertechnologie GmbH (now: 2oneLab GmbH, Darmstadt, Germany). The PBF-LB system is equipped with an Ytterbium fiber laser with a wavelength of 1070 nm and a maximum power of 250 W. The round base plate has a diameter of 110 mm. An F-Theta lens ensures a constant spot diameter across the processing area. During the building process, an Argon atmosphere with a remaining oxygen content of <0.1% in the processing chamber prevents oxidation. Optimized parameters from a previous study with a laser power of 250 W, a scanning speed of 900 mm/s, a hatch spacing of 150 µm, a layer thickness of 30 µm and a spot diameter of 40 µm were used for the PLF-LB process. The buildup process took place without preheating of the base plate. A common bidirectional line scanning strategy with a triple contour scan and a rotational angle of 67° of the hatching pattern of two subsequent layers was used.

Sample geometry

Two groups of samples were evaluated in this study, which are summarized in Table 2. To study geometric influences on the microstructure and the mechanical behavior, the first group consisted of representative geometric elements. The rectangular samples with a height of 50 mm were built with different cross sectional areas of 6x1, 6x2 and 6x6 mm² under varying construction angles of 45, 60 and 75° without the use of support structures. In the second group of samples, three-point bending beams with an optimized topology were manufactured as a demonstrator to study the global component behavior. The two dimensional design proposal for the bending beam was generated using the solver of the software Tosca 2019 from Dassault Systems (Vélizy-Villacoublay, France). An area reduction of 40% in a design space of 48x12 mm² was set as a boundary condition with the aim of a maximum stiffness of the part [9].

Table 2: Overview of the samples studied.

Group A – Bulk material	
Construction angles	45, 60 ,75°
Cross sectional areas	6x1, 6x2, 6x6 mm²
Experimental Methods	Microstructural analysis Small-scale tensile tests

Group B – Bending beams	
Dimension	48x12x12 mm³
Manufacturing route	PBF-LB PBF-LB+EDM
Experimental Methods	Micro-computed tomography Component tests

For a stable position of the bending beams during the component test, the design proposal obtained from the topology optimization was provided with shoulders at the sides. The derived design proposals were extracted to a constant thickness of 12 mm, which enables the manufacturing with two different routes, as depicted in Figure 1.

Figure 1: Manufacturing of the bending beams analyzed in this study.

To ensure manufacturability over both routes, a minimum wall thickness of 1.25 mm was additionally set as a boundary condition to the topology optimization algorithm. In route A, the bending beams were directly built in the PBF-LB process. Since the geometry of the design proposal contains regions which are built under different construction angles, as well as areas of different cross sectional areas, an inhomogeneous microstructure is expected within the parts. To avoid distortion, support structures were used on downskin surfaces with a construction angle of less than 45°. In route B, first a rectangular block of bulk material was manufactured in the PBF-LB process. The contour of the beam was then generated using electric discharge machining (EDM). Therefore, a homogeneous microstructure is expected within the parts.

Experimental Methods

Microstructural analysis

For microstructural analysis, representative samples of group A were ground with SiC paper and then polished using diamond pastes. Etching was performed in an aqueous solution of 2% NaOH for 85s. For evaluation of the microstructure, scanning electron microscopy was used. All of the images were captured normal to the building direction. In order to be able to resolve spatial inhomogeneities, the microstructure was analyzed in varying positions within the cross sections of the samples. Since gradients in microstructure can also occur across a single melt pool [10], the images were captured in the melt pool center to ensure comparability.

Tensile testing

The effects of inhomogeneous microstructure on mechanical material behavior were evaluated using tensile tests. The geometry of the tensile bars is shown in Figure 2. The tensile bars were taken at defined distances from the downskin surfaces of the printed rectangular samples in

group A using EDM. The tensile tests were performed at room temperature using an universal testing machine Z2.5 TN from ZwickRoell GmbH (Ulm, Germany) with a maximum load of 2.5 kN. The tests were conducted at a constant strain rate of 10^{-3}/s until fracture. A preload of 10N was applied. The strain was captured with digital image correlation using the software GOM Aramis (Carl Zeiss GOM Metrology GmbH, Braunschweig, Germany).

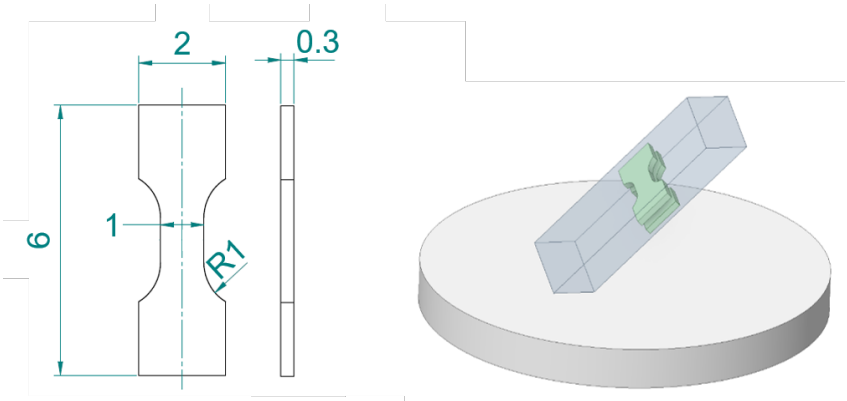

Figure 2: Geometry of the small-scale tensile bars in mm (left) and positions of the tensile bars in the printed bulk material (right).

Component behavior

In order to investigate the influence of inhomogeneous microstructure on the component behavior, three point bending tests were performed on the samples of group B (see Figure 3). The bending tests were carried out on an universal testing machine from ZwickRoell with a maximum load of 100 kN. The distance between the supporting pins was 48 mm. The loading pins and the supporting pins were rigid and had a diameter of 10 mm. The displacement of the specimens was determined with a tactile displacement transducer, which was placed centrally under the bending beams. The tests were performed at a displacement speed of 1 mm/min.

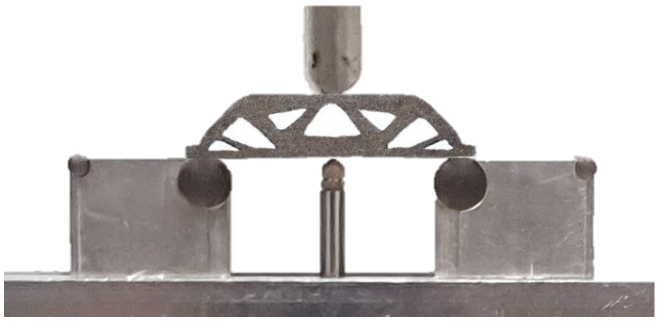

Figure 3: Experimental setup for the performed component tests.

Micro-computed tomography

In order to investigate the influence of defects on the component behavior, the fabricated bending beams were analyzed with micro-computed tomography (µCT). Therefore, the µCT-System PRECISION, developed by YXLON International GmbH (Hamburg, Germany) was used. The X-ray beam was generated at an acceleration voltage of 165 kV and a target current of 0.06 mA. The intensity of the X-rays was recorded using a Perkin Elmer XRD1620 AN flat panel

detector featuring a pixel pitch of 200 µm and an overall size of 2048 x 2048 pixels. The scanning was performed with a focus object distance (FOD) of 51.65 mm and a focus detector distance (FDD) of 913.92 mm, resulting in a voxel size of 11.3 µm. In each scan, 1860 projections were captured. The reconstruction of 3D images was performed through a filtered back projection (FBP) algorithm implemented in VGStudioMAX from Volume Graphics International GmbH (Heidelberg, Germany). For qualitative assessment of defect hotspots in the samples, projections of the minimum gray values were generated along the building direction using the thick slab algorithm of VGStudioMAX.

Results and discussion

Microstructural analysis

In Figure 4, two micrographs of a bulk sample with a dimension of 6x2 mm² and a construction angle of 45° are presented. The micrograph at the left was taken at 200 µm to the downskin surface, the one at the right at 1000 µm.

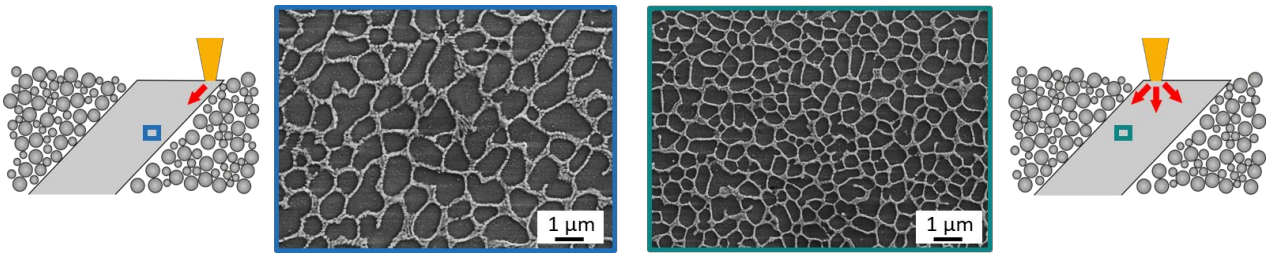

Figure 4: Gradient in Microstructure due to a local change of the cooling conditions.

Both micrographs show a cellular structure of primary crystallized Al and eutectic Si, which is typical for PBF-LB AlSi10Mg in the as-built state [2, 3]. However, the cellular structure in the left micrograph appears much coarser. It is commonly known from literature, that the cellular size in Al-Si alloys is strongly correlated to the cooling conditions, which can be expressed using the following formula [11]:

$$\lambda = a(G \times R)^{-n}$$

The product of the thermal gradient and the growth rate $(G \times R)$ is the cooling rate during solidification, λ is the cellular size, a and n are positive constants. Therefore, it can be concluded that areas with a bigger cellular size solidified at a lower cooling rate. As it is depicted in Figure 4, the heat dissipation during PBF-LB is limited especially on the downskin surface of overhanging parts. Therefore, a heat buildup is formed, which finally results in a local reduction of the cooling rate and thus a coarser microstructure [6, 7]. To analyze how strongly the effect affects different component geometries, the cell size of the bulk samples of group A was evaluated. For this purpose, microstructural images were taken from defined distances to the downskin surfaces. To ensure comparability, the images were taken from the melt pool center since the microstructure can change over the cross section of a melt pool [10]. To evaluate the cellular size, the captured microstructural images were first binarized with ImageJ. The evaluation of the cellular size then was performed with the ImageJ plugin MorpholibJ [12]. Figure 5 shows the results for specimens at different construction angles (left) as well as for different cross-sectional areas (right).

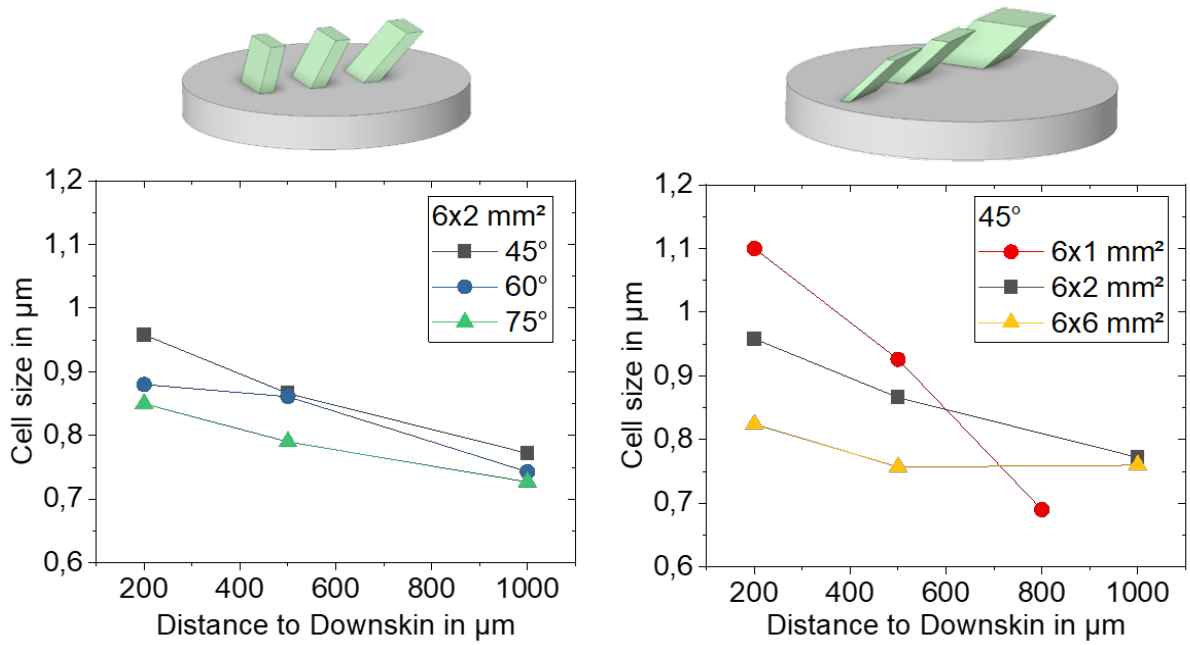

Figure 5: Influence of the construction angle (left) and of the cross sectional areas (right) on the cellular size in PBF-LB AlSi10Mg.

All samples show an increasing cellular size towards the downskin surface. This effect is amplified for a reduced construction angle as well as for a reduced wall thickness due to the limited heat dissipation during the PBF-LB process.

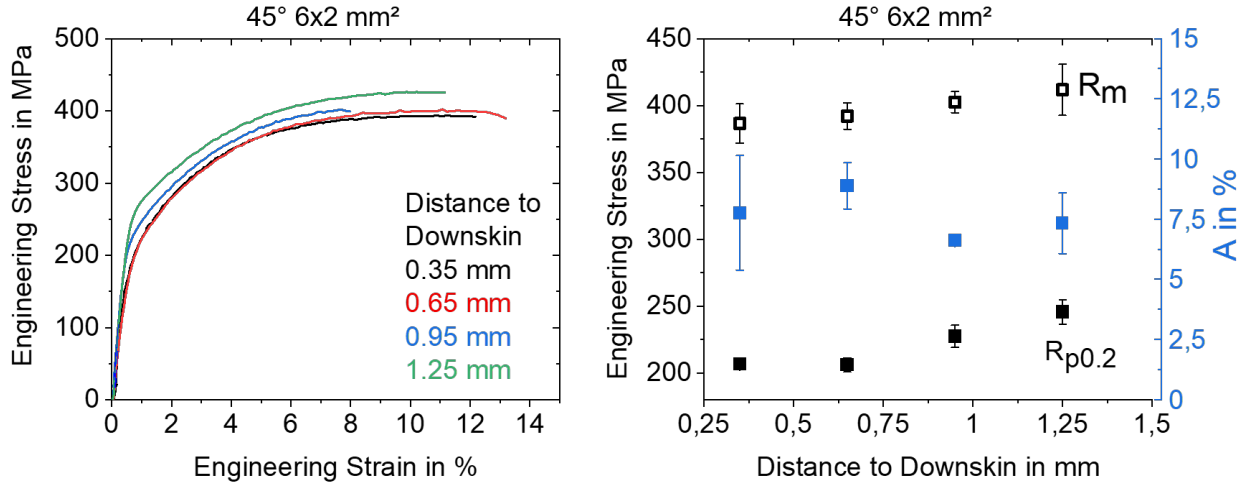

Figure 6: Representative stress-strain curves (left) and derived yield strength, tensile strength and elongation after fracture (right).

Tensile testing

In Figure 6 (left), representative stress-strain curves of tensile bars taken from defined distances from the downskin surface of a 6x2 mm² block built up at 45° are depicted. Figure 6 (right) shows the yield strength, tensile strength and elongation after fracture. The results were derived out of the recorded stress-strain curves according to the standard DIN EN ISO 6892-1 [13]. The stress-strain curves show an increase in yield strength and tensile strength with increasing distance from the downskin surface. This behavior can be related to the graded microstructure shown in the microstructure analysis. The cellular structure serves as barrier for dislocations and therefore contributes directly to the yield strength, which can be estimated with the Hall-Petch relationship [14, 15]. Furthermore, the inhomogeneous cellular size indicates changing solidification conditions across a component. Therefore, other strengthening mechanisms, such as the formation of Si precipitates and supersaturation in the solid solution can be influenced as well [14].

Figure 7 shows the influence of the construction angle (left) and the influence of the exposed cross-sectional area (right) on the local yield strength. The results show clearly that a smaller construction angle and a smaller exposed cross-sectional area lead to a larger gradient of the yield strength within one part. In general, the determined values for yield strength and tensile strength are comparable with the results of macroscopic tensile tests of PBF-LB AlSi10Mg from the literature [16]. However, the elongation after fracture does not show a clear correlation, as it is shown in Figure 6. It can be assumed that for Al-Si-Mg alloys, defects have a major influence on the elongation after fracture [17]. This is also shown on a representative optical image of the fracture surface of a tensile specimen (see Figure 8). Since the gauge volume of the tensile specimens is very small, variations in porosity between individual samples are to be expected, which therefore explains the higher variations regarding the elongation after fracture.

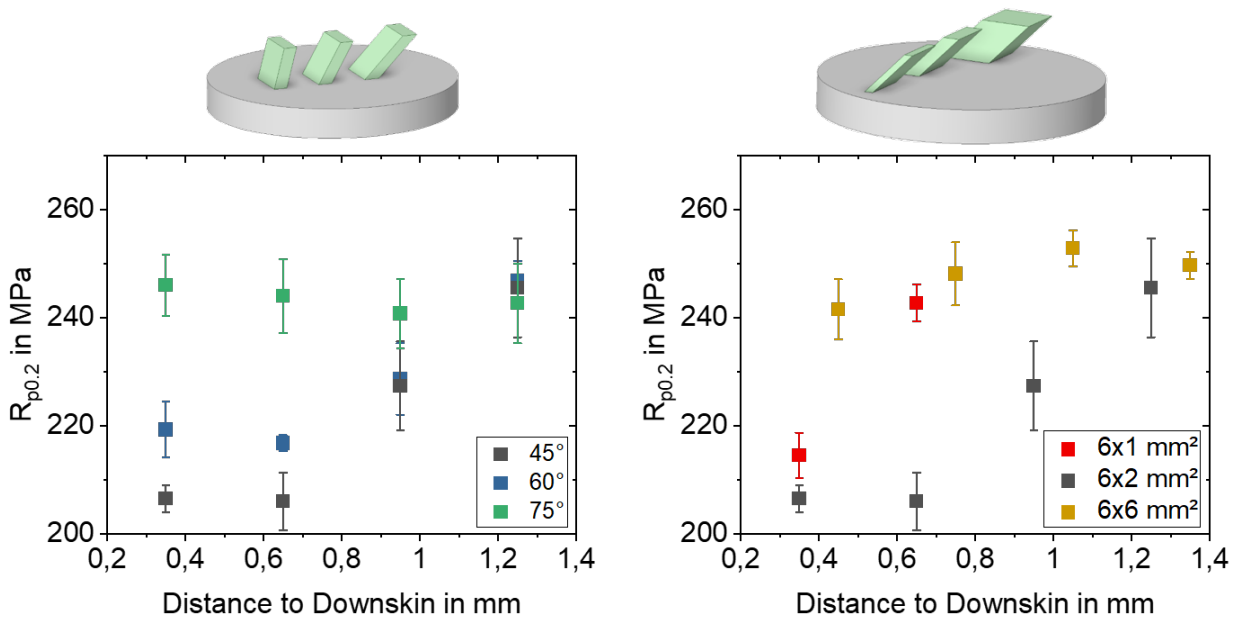

Figure 7: Influence of the construction angle (left) and of the cross sectional areas (right) on the local yield strength in PBF-LB AlSi10Mg.

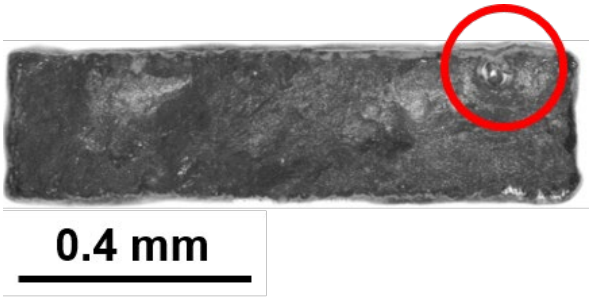

Figure 8: Optical image of the fracture surface of a small-scale tensile specimen with marked pore.

Micro-computed tomography

Figure 9 shows representative µCT images for the bending beams of each production route. To highlight the porosity, these are projections of the lowest gray values over 5 mm, which were generated using the thick slab algorithm implemented in VGStudioMAX. For the bending beam, which was manufactured directly in the PBF-LB process, a global porosity of 0.16% was determined. The PBF-LB + EDM bending beam shows a higher porosity of 0.62%. Due to the exposure of the larger surface area in the PBF-LB process, more process by-products such as spatter are formed. These can be larger than the powder particles and therefore lead to the formation of lack-of-fusion defects [18, 19]. Accordingly, the top and bottom surfaces of the beam produced directly in the PBF-LB process show locally increased porosity. The thin-walled component areas, on the other hand, exhibit low porosity regardless of the build angle.

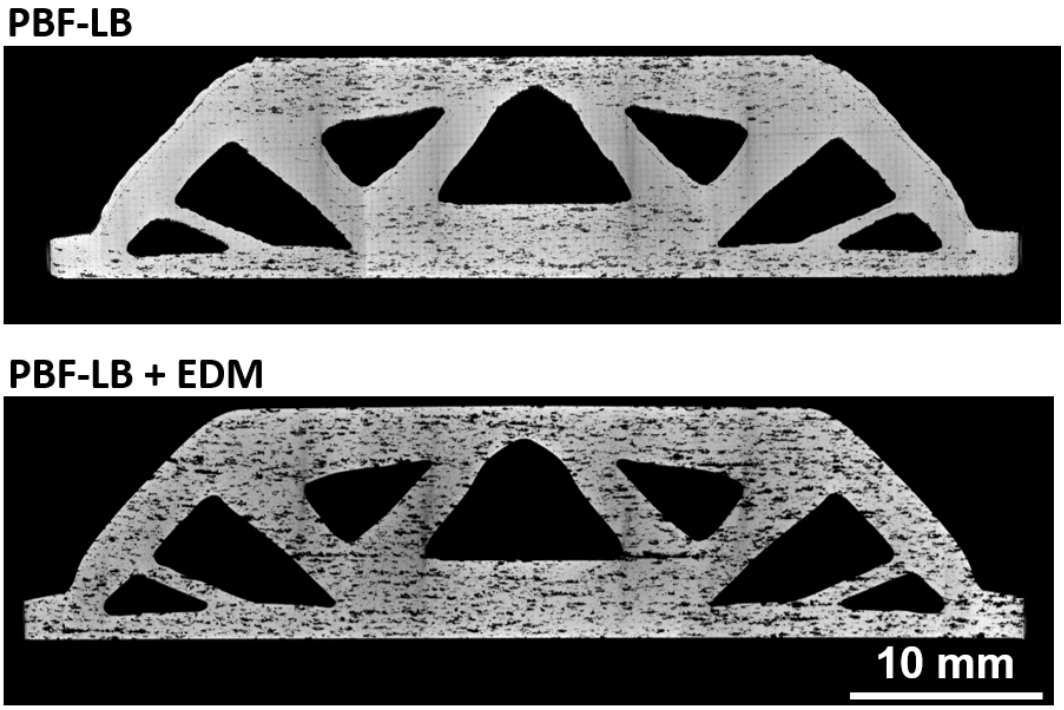

Figure 9: Projections of the lowest grey values over 5 mm from µCT images of representative bending beams.

Component behavior

The effects of the geometry-dependent mechanical material behavior were tested by means of component tests on three-point bending beams. Figure 10 shows the force-displacement curves of the tested components, Table 3 summarizes the results.

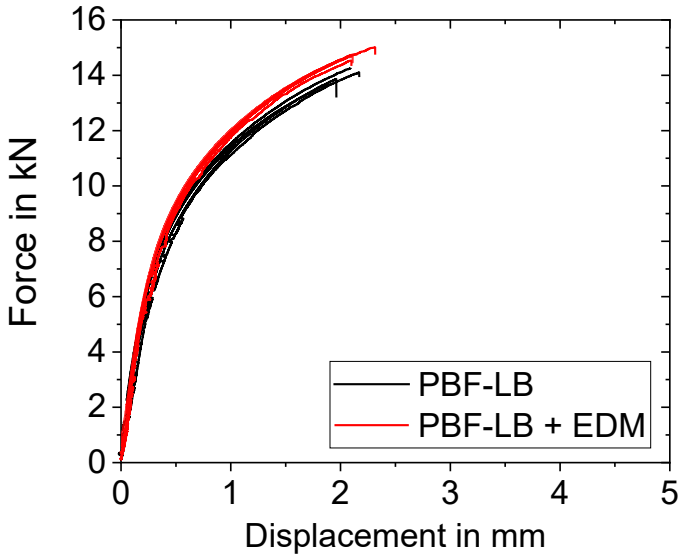

Figure 10: Force-displacement curves of the bending beams tested in this study.

Table 3: Results of the component tests.

Manufacturing route	Max. load in kN	Max. displacement in mm
PBF-LB	13,98 ± 0,26	2,03 ± 0,13
PBF-LB + EDM	14,74 ± 0,20	2,17 ± 0,10

Since the use of different routes to manufacture the beams can lead to deviations in terms of dimensional accuracy and thus influence the deformation behavior, comparability between the two manufacturing routes must be ensured. A corresponding check of the masses revealed a negligible difference of less than 0.5% between the bending beams of both manufacturing routes. Furthermore, the geometries of the bending beams were evaluated on the basis of the obtained µCT data. A surface analysis revealed maximum deviation of 0.1 mm between the two geometries for the upskin and vertical surfaces. Just at downskin surfaces, some local deviations of up to 0.3 mm were detected which could be attributed to powder adhesions on the beam, which was manufactured directly using PBF-LB.

The results obtained by the component tests, show clearly that the PBF-LB + EDM type bending beams have a higher strength than the bending beams built directly in the PBF-LB process, the maximum displacement appears to be similar. This behavior is not in accordance with the findings of the µCT analysis, therefore the microstructure needs to be taken into account. The design of the considered bending beams resulting from the topology optimization contains many thin-walled struts as well as many overhanging component areas. From the investigations carried out within the scope of this work, it can be concluded that different temperature fields are present in the structure of these component areas in the PBF-LB process. Particularly at the downskin surfaces

of thin-walled component areas, heat buildup occurs due to the insulating effect of the surrounding metal powder. The associated locally reduced cooling rate results in a coarsening of the microstructure, which ultimately influences the mechanical behavior.
In the case of the bending beams produced via the PBF-LB+EDM route, the generation of the component contour took place after the PBF-LB process, so that no overhanging or thin-walled areas were built up in this route.

Conclusions

In this study, the influence of inhomogeneous material properties on the mechanical behavior of additively manufactured components made of AlSi10Mg was investigated. For this purpose, representative geometric elements with different wall thicknesses were manufactured under different construction angles at first. A microstructural analysis revealed a coarsening of the microstructure towards the downskin area, which could be associated with a reduced dissipation of the process heat. By tensile tests on small-scale tensile specimens, the mechanical material behavior could be spatially resolved and related to the results of the microstructure analysis. In the second part of the study, the global component behavior was considered. By means of component tests on a topology-optimized demonstrator part, the influence of process-related inhomogeneous material behavior on the complete component behavior could be shown, which highlights the importance of considering local material data in the component design.

Acknowledgements

This research was funded by the German Research Foundation (DFG) within the Project "SLM-Topo: Entwicklung einer prozessspezifischen Topologieoptimierungsmethode für die additive Fertigung von Leichtbaustrukturen am Beispiel des SLM-Verfahrens" (Project number 399233791). The financial support for this research is gratefully acknowledged.

References

[1] Li, Y. and Gu, D. 2014. Parametric analysis of thermal behavior during selective laser melting additive manufacturing of aluminum alloy powder. *Materials & Design* 63, 856–867.

[2] Li, W., Li, S., Liu, J., Zhang, A., Zhou, Y., Wei, Q., Yan, C., and Shi, Y. 2016. Effect of heat treatment on AlSi10Mg alloy fabricated by selective laser melting: Microstructure evolution, mechanical properties and fracture mechanism. *Materials Science and Engineering: A* 663, 116–125.

[3] Liu, X., Zhao, C., Zhou, X., Shen, Z., and Liu, W. 2019. Microstructure of selective laser melted AlSi10Mg alloy. *Materials & Design* 168, S3, 107677.

[4] Kempf, A. and Hilgenberg, K. 2020. Influence of sub-cell structure on the mechanical properties of AlSi10Mg manufactured by laser powder bed fusion. *Materials Science and Engineering: A* 776, 8, 138976.

[5] Dong, Z., Zhang, X., Shi, W., Zhou, H., Lei, H., and Liang, J. 2018. Study of Size Effect on Microstructure and Mechanical Properties of AlSi10Mg Samples Made by Selective Laser Melting. *Materials (Basel, Switzerland)* 11, 12.

[6] Liu, M., Takata, N., Suzuki, A., and Kobashi, M. 2020. Development of gradient microstructure in the lattice structure of AlSi10Mg alloy fabricated by selective laser melting. *Journal of Materials Science & Technology* 36, 106–117.

[7] Yue, D., Li, D., Zhang, X., Chen, B., Qin, R., and Wang, Z. 2023. Tensile behavior of AlSi10Mg overhanging structures fabricated by laser powder bed fusion: Effects of support structures and build orientation. *Materials Science and Engineering: A* 880, 2, 145375.
[8] Englert, L., Czink, S., Dietrich, S., and Schulze, V. 2022. How defects depend on geometry and scanning strategy in additively manufactured AlSi10Mg. *Journal of Materials Processing Technology* 299, 117331.
[9] Holoch, J., Lenhardt, S., Revfi, S., and Albers, A. 2022. Design of Selective Laser Melting (SLM) Structures: Consideration of Different Material Properties in Multiple Surface Layers Resulting from the Manufacturing in a Topology Optimization. *Algorithms* 15, 3, 99.
[10] Patakham, U., Palasay, A., Wila, P., and Tongsri, R. 2021. MPB characteristics and Si morphologies on mechanical properties and fracture behavior of SLM AlSi10Mg. *Materials Science and Engineering: A* 821, 3, 141602.
[11] Matyja, H., Giessen, B. C., and Grant, N. J. 1968. The effect of Cooling Rate on the Dendrite Spacing in Splat-Cooled Aluminium Alloys. *J. Inst. Met.,* 96, 30–32.
[12] Legland, D., Arganda-Carreras, I., and Andrey, P. 2016. MorphoLibJ: integrated library and plugins for mathematical morphology with ImageJ. *Bioinformatics (Oxford, England)* 32, 22, 3532–3534.
[13] *DIN EN ISO 6892-1:2020-06, Metallische Werkstoffe_- Zugversuch_- Teil_1: Prüfverfahren bei Raumtemperatur (ISO_6892-1:2019); Deutsche Fassung EN_ISO_6892-1:2019*. Beuth Verlag GmbH, Berlin.
[14] Hadadzadeh, A., Baxter, C., Amirkhiz, B. S., and Mohammadi, M. 2018. Strengthening mechanisms in direct metal laser sintered AlSi10Mg: Comparison between virgin and recycled powders. *Additive Manufacturing* 23, 108–120.
[15] Ghio, E. and Cerri, E. 2022. Additive Manufacturing of AlSi10Mg and Ti6Al4V Lightweight Alloys via Laser Powder Bed Fusion: A Review of Heat Treatments Effects. *Materials (Basel, Switzerland)* 15, 6.
[16] Zhang, J., Song, B., Wei, Q., Bourell, D., and Shi, Y. 2019. A review of selective laser melting of aluminum alloys: Processing, microstructure, property and developing trends. *Journal of Materials Science & Technology* 35, 2, 270–284.
[17] Cáceres, C. H. and Selling, B. I. 1996. Casting defects and the tensile properties of an AlSiMg alloy. *Materials Science and Engineering: A* 220, 1-2, 109–116.
[18] Anwar, A. B. and Pham, Q.-C. 2018. Study of the spatter distribution on the powder bed during selective laser melting. *Additive Manufacturing* 22, 1, 86–97.
[19] Liu, Y., Yang, Y., Mai, S., Di Wang, and Song, C. 2015. Investigation into spatter behavior during selective laser melting of AISI 316L stainless steel powder. *Materials & Design* 87, 9–12, 797–806.